Controlling S_1/S_0 Decay and the Balance between Photochemistry and Photostability in Benzene: A Direct Quantum Dynamics Study†

Benjamin Lasorne,‡ Michael J. Bearpark,‡ Michael A. Robb,*,‡ and Graham A. Worth*,§

Department of Chemistry, Imperial College London, London SW7 2AZ, U.K., and School of Chemistry, University of Birmingham, Birmingham B15 2TT, U.K.

Received: April 29, 2008; Revised Manuscript Received: July 10, 2008

In this work, we investigate general mechanistic principles that control reaction selectivity following S_1/S_0 internal conversion in benzene. A systematic relationship is drawn between the varying topology of an extended seam of conical intersection and the balance between two competitive radiationless decay channels: photophysical (benzene reactant regeneration) and photochemical (prefulvene product formation). This is supported by a model quantum dynamics study, using a direct dynamics approach based on variational multiconfiguration Gaussian wavepackets, where initial excitation of specific vibrational modes is designed to generate dynamical pathways that reach selected targets regions of the seam. High-energy regions of the seam are found to be sloped and in favor of the photophysical channel, while lower-energy regions are peaked and give access to the photochemical channel. This changeover could in principle be exploited to define targets for optimal control, by exciting different combinations of specific vibronic levels in S_1, accessing different regions of the seam, and giving different products.

1. Introduction

Optimal control studies of molecular processes use closed loop techniques to achieve maximum efficiency when designing a laser pulse that will drive the system to a targeted outcome through a "black box" mechanism.[1−3] Simulations based on optimal control theory[4,5] monitor the wavepacket evolution induced by a time-dependent Hamiltonian, but the effect of the resultant, often complicated, pulse shapes is not easy to decipher. Few attempts have been made at connecting experiments to simulations in this context (see, e.g., ref 6). For large molecules in particular, the level of quantum chemistry calculations achievable may not be accurate enough to provide ready-to-use ab initio designed laser pulses, as can be done for small systems.[7]

In contrast, intelligent control is the challenge to use theory to rationalize and thus aid experiments. This approach assumes that the reaction selectivity is governed by simple mechanistic principles and that tailored laser pulses can be decoded in terms of specific dynamical pathways on potential energy surfaces (PESs). In this spirit, a very recent experimental investigation on the photoisomerization of a cyanine[8] has provided support for such control possibilities, inferred from previous theoretical studies.[9] The theoretical study had suggested that the keystone for controlling the photoreactivity was targeting specific regions of molecular geometries corresponding to specific parts of the conical intersection seam (see, e.g., ref 10 and references therein) joining the S_0 and S_1 PESs: different crossing points lead to different products on the ground-state surface (see also refs 11 and 12). Accessing specific geometries can be correlated to the excitation of specific vibrational modes by the laser pulse. Similar concepts were used in a recent study of the mode-dependence of the photoreactivity of chromenes.[13] Intelligent control is also relevant for infrared-laser-driven control of ground-state reactivity where mode-selective intramolecular vibrational energy redistribution (IVR) must be rationalized (see, e.g., refs 14 and 15).

SCHEME 1: Primary Event in the S_1 Photochemistry of Benzene

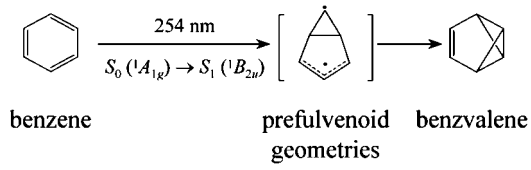

If intelligent control is based on the characteristics of a conical intersection seam, the first step should be a prediction of the vibrational modes that must be stimulated in the electronic excited state to enable the system to reach a particular crossing region. Such regions must be characterized as potential targets able to alter the reaction selectivity subsequent to radiationless decay to the electronic ground state. In this work, we have applied this strategy to the S_1/S_0 decay in benzene. Dynamical pathways connecting various initial conditions to specific targets have been explored by quantum dynamics calculations. The relevant vibrational modes have been identified in a previous work,[16] as further recalled below.

In the S_1 spectroscopy of benzene, the so-called "channel 3" process represents the well-known radiationless decay route (photophysical and/or photochemical) that quenches fluorescence above a vibrational excess of 3000 cm^{-1} (see refs 17 and 18 and references therein). Experiments show that S_1 benzene can produce a small amount of photoisomers after deactivation.[19] The quantum yield of the primary photoproduct, viz. benzvalene (Scheme 1), increases with increasing excess energy but stays very low. The other photoproduct, viz. fulvene, is assumed to be formed by secondary isomerization of benzvalene. Thus, there must be a photochemical pathway that will account for

† Part of the Sason S. Shaik Festschrift.

* Corresponding authors. E-mail: mike.robb@imperial.ac.uk (M.R.) and g.a.worth@bham.ac.uk (G.A.W.).

‡ Imperial College London.

§ University of Birmingham.

10.1021/jp803740a CCC: $40.75
Published on Web 10/01/2008

production of S_0 benzvalene (and also, at least partly, for fluorescence quenching).

A static photochemical mechanism (see Figure 1) has been characterized by Palmer et al.[17] and supported by semiclassical trajectories in previous work.[20] Starting from the Franck−Condon (FC) region, the system follows a reaction path that must overcome an S_1 transition barrier before reaching the S_1/S_0 conical intersection (see also ref 21). The presence of a transition barrier before the S_1/S_0 crossing is in agreement with the observed 3000 cm^{-1} threshold in channel 3, under which vibrational states in S_1 are long-lived. Internal conversion leads then to the prefulvene intermediate that is a shallow minimum embedded in a flat plateau on the S_0 PES. From there the reaction path branches, and the system can either return to benzene or isomerize to benzvalene.

In Figure 1, the S_1/S_0 conical intersection is represented as a point. This picture (the "sand-in-the-funnel" model) is somewhat misleading for benzene, as it is for any molecule where an extended seam of conical intersection is energetically accessible (see, e.g., discussion in ref 12). The conical intersection actually corresponds here to a collection of structures that lie on a 28-dimensional hyperline, the seam of intersection between the two PESs. The minimum of the seam (the point shown in Figure 1) has been characterized as a prefulvenoid geometry corresponding to a peaked topology:[17] the gradients of the intersecting surfaces are not parallel. This can be related to the presence of the S_1 prefulvenoid transition structure (TS) on the way to the crossing, which makes the S_1 PES bend downhill at this crossing. We will show that other, energetically accessible, parts of this seam can be found along a breathing deformation from this prefulvenoid geometry, and the topology changes from peaked, near the S_1 TS, to sloped (parallel gradients), at higher energies, avoiding the S_1 TS and associated gradient sign change (see Figure 2). Structures other than the minimum of the seam can thus be accessed, and the purpose of the present work is to explore systematically the S_1 and S_0 coupled PESs of benzene in order to relate the features of the S_1/S_0 seam of intersection to the possible pathways for radiationless decay. This knowledge could be useful in the context of laser-driven control of photochemical reactivity if it helps to design a laser pulse that selectively enhances either regeneration of benzene or production of benzvalene, as illustrated in Figure 2.

The most important feature for controlling internal conversion in benzene is the following. If there is no initial momentum (FC conditions), the system will follow the negative of the S_1 gradient (breathing coordinate), toward the S_1 minimum (expanded D_{6h} geometry), and oscillate in this well. If sufficient momentum could be given to the photoactive prefulvenic coordinate (out-of-plane half-chair deformation), then decay would occur to S_0 at an expanded prefulvenoid geometry where the S_1/S_0 crossing is sloped, and no product would be observed (photophysical deactivation, i.e., photostabilization). This is illustrated by the effect of the hypothetical laser pulse 1 in Figure 2. However, if sufficient momentum were initially also added into the breathing coordinate so that benzene moved in the direction opposite to the S_1 minimum, i.e., ring compression, then decay would occur near the S_1 prefulvenoid TS, where funneling (dynamically) toward the S_0 prefulvenoid region is possible (photochemical pathway; see the effect of the hypothetical laser pulse 2 in Figure 2). In this, one of the main factors expected to control reactivity is the topology of the conical intersection region (within the seam) that was targeted. This hypothesis, which we believe is general, based on previous studies of various systems,[9,11,12,22−25] has been tested here on benzene using quantum dynamics calculations to probe dynamical pathways. In order to form benzvalene, the system must be driven to the seam at a point where the conical intersection is peaked, which happens in the vicinity of the S_1 prefulvenoid TS. This requires combining the breathing coordinate (compression) and the prefulvenic coordinate into a dynamical reaction coordinate (see Figure 2).

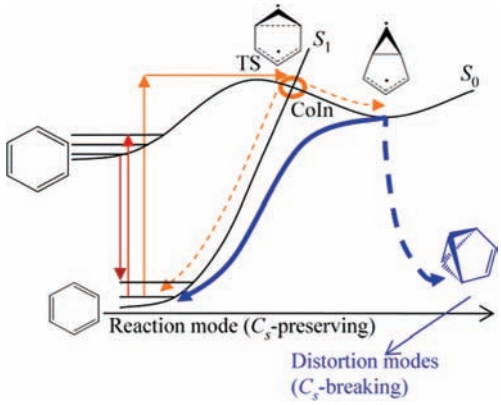

Figure 1. S_1 benzene photochemistry: S_1/S_0 internal conversion can lead back to S_0 benzene or generate the S_0 intermediate prefulvene, which in turn can regenerate S_0 benzene or form S_0 benzvalene.

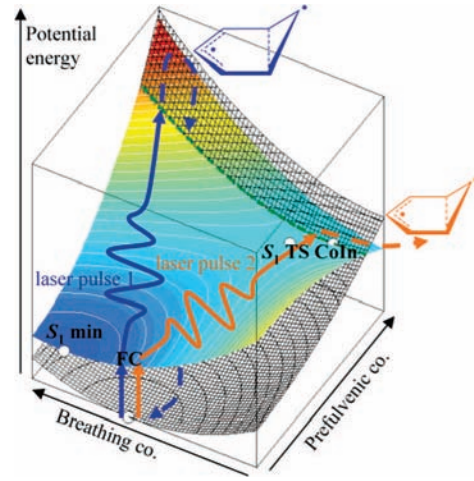

Figure 2. Hypothetically controlling the S_1 photochemistry of benzene: different laser pulse sequences lead to crossing the S_1/S_0 intersection seam in different places, modifying the reactivity. For example, pulse 1 leads to regeneration of benzene at a sloped conical intersection (photophysics), and pulse 2 allows for production of benzvalene at a peaked conical intersection (photochemistry). The seam between both crossing PESs is indicated with a dashed line.

In this work, targeting a point on the seam was achieved computationally by giving a specific extra momentum to the initial wavepacket. Here, we are not concerned with how a wavepacket can be designed in experiments, where selection rules are important, but use it merely as an exploration tool. This has provided information on the nature of the dynamical pathways optimal for enhancing internal conversion toward the formation of products. They were calculated with the direct dynamics variational multiconfiguration Gaussian wavepacket (DD-vMCG) approach. The vMCG method has been successfully tested in the context of nonadiabatic photochemistry, and the direct dynamics version appears to be a reliable approach to deal with nonadiabatic transitions between coupled electronic states, while keeping the advantage of calculating the PESs and nonadiabatic couplings on-the-fly.[26−30]

The work is organized as follows. The active coordinates for dynamics are documented in section 2. Computational details

about quantum chemistry calculations and quantum dynamics propagations are given in section 3. The extended seam of conical intersection is documented in section 4. Results of dynamics calculations are presented in sections 5 and 6, and concluding remarks and outlook are gathered in section 7.

2. The Relevant Vibrational Modes and Active Coordinates

In the static mechanism describing the $S_1 \leftarrow S_0$ photochemistry of benzene[17] (see Scheme 1 and Figure 1), the S_1/S_0 conical intersection minimum (noted as CoIn in Figure 1) is a C_s prefulvenoid structure (a three-electron cyclopropenoid ring coupled to an allylic moiety), a precursor of the prefulvene intermediate that lies on a flat plateau of very similar structures—namely, a shallow minimum, a TS, and a second-order saddle point—leading either to direct formation of benzvalene or to ground-state regeneration of benzene (see Figure 1). The CoIn point is accessed from the FC point through a rather flat TS on S_1 that correlates diabatically with the prefulvenoid plateau: the transition vector resembles the gradient difference and describes formation of the new CC bond in prefulvene, as well as an out-of-plane ring bending that leads to the typical half-chair structure of all prefulvenoid geometries.

Selecting a relevant subset of active coordinates is an important matter in applying intelligent control to organic photochemistry for two reasons. First, reducing the number of degrees of freedom is a practical way to treat larger systems computationally.[31−35] Second, predicting the optimal frequency composition of a laser pulse is easier when dealing with only a subset of active modes. The selection of modes was performed automatically using a new methodology[16] based on a quantum chemical approach originally developed for analytically calculating the quadratic representation of a conical intersection[36−39] and applied here at the FC point.

The gradient-difference and interstate-coupling vectors calculated at a point where the energy difference between S_1 and S_0 is finite define a pseudobranching plane. The Hessian of the energy difference is calculated analytically within the state-averaged CASSCF method. It is projected out of the pseudobranching plane before diagonalization. In benzene, this leads to 28 normal modes of the energy difference, orthogonal to the pseudobranching plane. A negative energy-difference Hessian eigenvalue corresponds to a smaller curvature of the S_1 PES than the S_0 PES. Modes with the largest negative eigenvalues are thus the most relevant to facilitate access to the S_1/S_0 seam of conical intersection, as they close the energy gap between states most quickly. They are called photochemically active modes. Along with the gradient-difference vector, they describe the shortest route to the conical intersection seam, provided that terms of third-order or more do not take over along the corresponding displacements drawn from the FC point.

The relevant vibrational modes were selected as (i) the gradient-difference vector at the FC point (a_{1g}-direction of the S_1 driving force, since the S_0 gradient is zero), (ii) the interstate-coupling vector at the FC point (b_{2u}-direction of the pseudo-Jahn−Teller effect[40,41]), and (iii) some of the most relevant photochemically active modes (large negative eigenvalues and deformations localized on the C_6-ring rather than on peripheral H nuclei). These energy-difference modes were compared to the set of 30 normal modes of vibration calculated at the D_{6h} geometry of the benzene minimum on S_0 (throughout the paper, the Wilson scheme[42] will be used to number vibrational modes). It was found that the simplest model subspace suitable for dynamics simulations was 5-dimensional (5D). The five S_0 normal modes that best describe the five active energy-difference modes are the breathing mode $1a_{1g}$ (ν_1), the Kékulé mode $1b_{2u}$ (ν_{15}), and the three out-of-plane modes $1b_{2g}$ (ν_4) and the degenerate pair $1-2e_{2u}$ (ν_{16}). These are illustrated in Figure 3. From the D_{6h} S_0 minimum, deformations along the latter three modes lead respectively to chair, boat, and twist geometries that can be combined to keep five C nuclei in a plane with one out-of-plane (half-chair geometry). They are thus involved in the prefulvenic coordinate, needed to go from the FC point to prefulvenoid structures implied in the state crossing (see Scheme 1 and Figure 1).

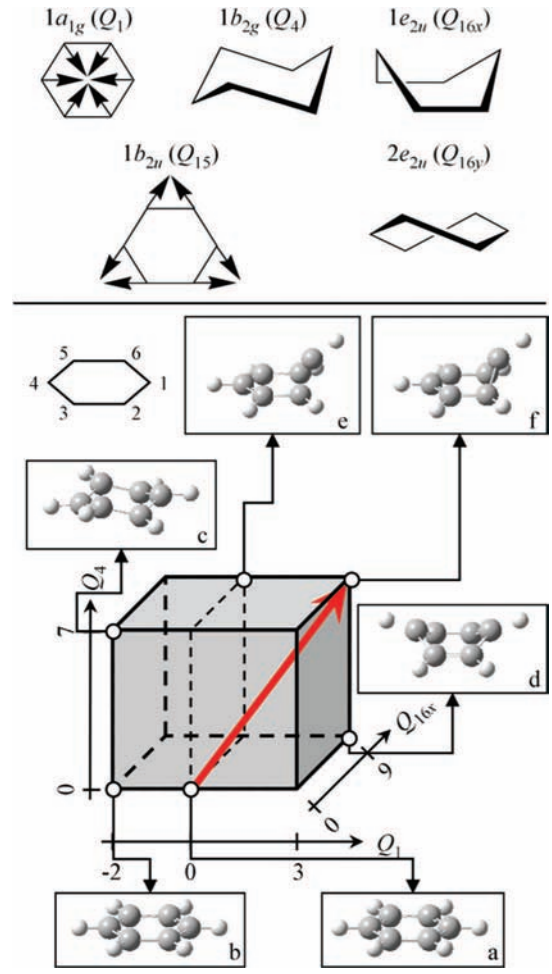

Figure 3. Upper panel: the five normal modes defining the 5D model subspace used for dynamics calculations (coordinates Q_j measure the magnitude of nuclear displacements along the corresponding modes). The three out-of-plane modes are not represented by the displacement arrows but by the resulting distortions (chair, boat, and twist). Our method for choosing the active modes is discussed is ref 16. Lower panel: some examples of molecular geometries specified by a set of values $\{Q_1, Q_4, Q_{16x}\}$ (all other displacements are set to zero). At the origin, {0, 0, 0}, the FC point is a D_{6h} geometry (a) with bond lengths CC = 1.40 Å; {−2, 0, 0} corresponds to a stretched D_{6h} geometry (b) with all CC = 1.44 Å; {−2, 7, 0} describes a chair geometry (c) with all CC = 1.47 Å, and all dihedral angles CCCC = ±41.9°; {3, 0, 9} describes a boat geometry (d) with C_1C_2 = 1.44 Å, C_2C_3 = 1.34 Å, and $C_2C_3C_4C_5$ = 45.2°; {0, 7, 9} and {3, 7, 9} correspond to half-chair (prefulvenic) geometries: (e) with C_1C_2 = 1.64 Å, C_2C_3 = 1.43 Å, C_3C_4 = 1.41 Å, $C_1C_2C_3C_4$ = 37.2°, and $C_2C_3C_4C_5$ = 4.6° for {0, 7, 9} and (f) with C_1C_2 = 1.59 Å, C_2C_3 = 1.38 Å, C_3C_4 = 1.35 Å, $C_1C_2C_3C_4$ = 38.3°, and $C_2C_3C_4C_5$ = 4.8° for {3, 7, 9}. The red arrow illustrates an example of **k** vector (see sections 4−6) where $\{k_1, k_4, k_{16x}\}$ is proportional to {3, 7, 9}.

In the following, Q_j will be used to represent two things: the name of a *normal mode* (direction of a molecular vibration in

TABLE 1: Frequency-Mass-Weighted Normal Coordinates and Electronic Energies of the Main Critical Points,[a] Optimized and Vertically Projected at the CAS(6,6)/6-31G* Level

	Bz S_0 min	sBz S_1 min	TS S_1	CoIn S_1/S_0	pF S_0 TS	pF S_0 SP2	pF S_0 min	Bv S_0 min	DBz S_0 min
Q_1	0	−1.86	1.62	3.10	6.12	6.50	7.32	12.99	8.84
Q_4	0	0	5.14	6.28	8.88	9.43	9.76	11.97	0
Q_{15}	0	0	0	0	0	0	0	−1.14	0
Q_{16x}	0	0	7.20	8.16	9.80	10.49	11.09	10.64	14.31
Q_{16y}	0	0	0	0	0	0	0	−6.14	0
E_0/eV	0	0.21	3.87	5.61(4.14)	5.02	5.23	4.95	3.86	3.66
E_1/eV	4.99	4.78	5.56	5.61 (6.99)	8.22	8.32	7.90	12.00	12.04

[a] Benzene (Bz) S_0 minimum, stretched benzene (sBz) S_1 minimum, S_1 transition structure (TS), S_1/S_0 conical intersection (CoIn) minimum (0.5:0.5 state-averaged), prefulvene (pF) S_0 TS, prefulvene S_0 second-order saddle-point (SP2), prefulvene S_0 minimum, benzvalene (Bv) S_0 minimum, and Dewar benzene (DBz) S_0 minimum. Energy values within parentheses for CoIn are those of the projected point (5D subspace). In the constrained 5D subspace, S_0 and S_1 do not intersect at the 5D-projected point but do for more bent prefulvenoid structures with larger values of Q_4 and Q_{16x} and higher energies (a typical scaling factor of about 1.5 for both kinds of quantities). In the more flexible 9D subspace, the energy gap at the projected point is reduced (see Supporting Information).

the configuration space of the nuclei, given as a unit vector in mass-weighted Cartesian coordinates) and the numerical value, i.e., *normal coordinate*, of a given nuclear displacement along this direction, having zero value at the D_{6h} S_0 minimum. Normal coordinates are linear combinations of Cartesian coordinates of the nuclei, which are a convenient set of vibrational coordinates for quantum dynamics. A particular set of values $\{Q_j\}$ for the 30 normal coordinates represent a unique molecular geometry (point in the configuration space of the nuclei), and can be transformed into internal coordinates such as bond lengths and angles. The 5D subspace used in dynamics calculations simply means that inactive coordinates are frozen ($Q_j = 0$), while the five active coordinates, $\{Q_1, Q_4, Q_{15}, Q_{16x}, Q_{16y}\}$, vary under this constraint. In terms of trajectories, the evolution of the nuclei will be represented by the motion of a point in this 5D $\{Q_j\}$ space.

Table 1 lists the geometries and energies of the various important structures that may act as descriptors of the dynamics and form targets for enhancing the efficiency of radiationless decay. Frequency-mass-weighted dimensionless normal coordinates were used for practical reasons. Here, only the values of the five active coordinates are given. The critical points do not actually belong to the 5D subspace, as inactive coordinates may not be zero. However, for every $\{Q_j\}$ defining a given structure in the full space, the corresponding projection onto the 5D subspace (all coordinates set to zero but the active ones) defines an approximate structure resembling the original one. This approximation is relevant because the active coordinates were specifically chosen for describing the main features of the photochemical reaction path.

In particular, the adiabatic PESs do not intersect at the 5D-projected geometry of the minimum of the seam (CoIn point in Table 1). However, we checked that the diabatic surfaces do intersect along a subspace that is the projection of a very accessible part of the actual adiabatic seam in the full space (same values of the active coordinates, zero values for the remaining coordinates). Along this projected seam, the 5D-constrained adiabatic surfaces are shaped as a sloped avoided crossing extended along Q_1 and localized around $Q_4 \approx 6$ and $Q_{16x} \approx 8$ (similar to the CoIn point, minimum of the intersection seam). This is precisely where transfers of electronic population were observed in the quantum dynamics calculations.

In terms of dynamics, a diabatic trapping should happen in the sloped region of the seam, whereas a diabatic crossing is expected in the peaked region (see Figure 2). To increase reactivity, the obvious aim is thus to hit the intersection seam and then move on S_0 toward values of $\{Q_j\}$ defining structures close to that of prefulvene (pF S_0 min point in Table 1). In the 5D subspace, this topological feature will translate into a more or less sloped avoided crossing, thus resulting in wavepackets being bounced back early in the case of a nonreactive transition and having more time to travel in the direction of prefulvene for a reactive transition, before being eventually bounced back too. Any long-term dynamics is thus impossible to interpret in 5D, as this would require additional degrees of freedom for the potential energy to be sufficiently relaxed in the region of products. The discussion of results will therefore be based on short-term dynamics.

A more refined 9D model was also examined, allowing more flexibility of the ring. It includes additionally four in-plane modes (identified as the next relevant photoactive modes[16] after the five modes used in the 5D model): the degenerate pair $1-2e_{2g}$ (ν_6)—a quinoidic rectangular deformation and its antisymmetrical rhomboidal counterpart—involved in the Herzberg–Teller effect that makes the forbidden electronic transition from S_0 ($^1A_{1g}$) to S_1 ($^1B_{2u}$) possible[43] and the $1-2e_{1u}$ (ν_{18}) trapezoidal modes, which enable the formation of the prefulvenoid CC bond (see Figure 1). Some results are presented in section 6. More details are given in the Supporting Information.

3. Computational Details

Direct Quantum Dynamics Method. At conical intersections, the nuclear and electronic motions are coupled by what is termed nonadiabatic coupling. Strong quantum effects characterize such PES regions. They influence the nuclear motion and subsequently the photochemical mechanism. To correctly describe nonadiabatic processes, it is necessary to solve the time-dependent Schrödinger equation for the nuclear motion.[44]

Traditional quantum dynamics methods, which use fitted PESs mapped onto a multidimensional grid, are, however, expensive and applicable only to rather small systems (typically no more than four atoms). The multiconfiguration time-dependent Hartree (MCTDH) scheme[45−49] has pushed the limit up to seven atoms for ground-state chemical processes,[50−52] nine for ground-state vibrational spectroscopy,[53] and eight to 10 for vibronic spectroscopy.[54,55] However, nonadiabatic photochemical processes involving large-amplitude motions (such as photoisomerizations) have not been treated yet with this approach.

In contrast, direct dynamics calculates the PES on-the-fly where and when it is needed, using quantum chemistry calculations. Gaussian wavepackets are localized in space so that a local harmonic approximation (LHA) is a reasonable representation of the PES around their center.[56] This can be

obtained directly from electronic structure calculations. On-the-fly Gaussian wavepacket dynamics is thus a viable way of carrying out direct quantum dynamics (for recent reviews see refs 57 and 30. Direct dynamics implementations have been reported in the form of the ab initio multiple spawning method (AIMS),[58−61] and more recently the direct dynamics variational multiconfiguration Gaussian wavepacket (DD-vMCG) method used here.[26−29]

The vMCG equations of motion come from the same theoretical background as the standard MCTDH equations and have been implemented in a development version of the Heidelberg MCTDH package.[62] By comparison with accurate wavepacket calculations, vMCG has been shown to provide a good description of the dynamics of a molecular system using only a small basis set and subsequently a small number of parameters.[26,63] The general working equations of the vMCG method can be found in refs 26, 64, 30, and 29 They are recalled in the Supporting Information. The direct dynamics implementation has been presented elsewhere.[27,28] It benefits from using a simple database as data storage that grows on-the-fly to save unnecessary PES calculations. The database is a sequence of file records, each consisting of a molecular geometry and the corresponding LHA representation of the adiabatic PESs (energies gradients, and Hessians). For each geometry generated by the equations of motion, data are either read and extrapolated or calculated and written. Further details are given in the Supporting Information.

On-the-Fly PES Calculations. For the DD-vMCG method, the LHA representation of the PESs requires the calculation of the energy and first and second derivatives of the S_1 and S_0 adiabatic surfaces at the center of each GWP in the wavepacket expansion. When required, the S_1 and S_0 adiabatic PESs are evaluated on-the-fly using quantum chemistry calculations. We used a simple form of the regularized diabatic states method of Köppel et al.[65] (see also ref 26 for more details about the implementation) to transform the adiabatic information from the quantum chemistry calculations into the LHA expansion of both diabatic PESs and the coupling function.

A development version of the Gaussian program[66] was interfaced with the quantum dynamics code here. The C_6H_6 system was described using a complete active space self-consistent field (CASSCF) wave function with a 6-31G* basis set. An active space of six electrons spread over six π-molecular orbitals was used. The CAS space was initially obtained at the D_{6h} S_0 equilibrium geometry. The active space for the center geometry of each GWP was then propagated along the quantum trajectory, i.e., the guess for a CASSCF calculation is the active space of the last calculation performed for the GWP.

The configuration space was also divided up into three regions depending on the gap ΔE between the surfaces. Regions 1, 2, and 3 correspond respectively to $\Delta E < 0.1$ eV, $0.1 < \Delta E < 0.5$ eV, and $\Delta E > 0.5$ eV. In region 3, which is away from the intersection, full CASSCF calculations were done, optimizing to a particular state. In region 2, approaching the intersection, state-averaged CASSCF was used with a weight of 0.5:0.5 for the two states. Very close to the intersection, in region 1, no new calculations were made, and the surfaces simply updated until the gap grew large enough once more.

Gaussian Wavepacket Simulations. The initial wavepacket was a 5D product of Gaussian functions representing the vibrational ground state of the 1D harmonic oscillators corresponding to the subset of active coordinates. The frequencies were obtained from CASSCF calculations performed at the S_0 equilibrium geometry of benzene. The diabatic states were chosen to coincide with the adiabatic states S_1 and S_0 at the geometry of the S_1/S_0 conical intersection minimum and also at the FC point. Thus, the wavepacket, placed at the FC point at time $t = 0$ on the upper diabatic state, is initially on S_1.

This initial wavepacket was given additional average momentum, $\mathbf{p} = \hbar\mathbf{k}$, along a chosen direction by multiplying the real-valued multidimensional Gaussian function by the spatial phase factor exp ($i\,\mathbf{k}\cdot\mathbf{Q}$), where the $\mathbf{k}$ vector has components with magnitude along the normal coordinates, collectively denoted $\mathbf{Q}$ (frequency-mass-weighted dimensionless displacements from the FC point, as defined in section 2). The remaining inactive degrees of freedom can be viewed as spectator modes, unchanged by the electronic excitation and uncoupled to the dynamics.

In the vMCG approach, the initial wavepacket is used as a generic GWP to define the rest of the basis set. These functions are generated around the original function with the same widths, but shifted along each coordinate so that the overlap between any two functions is less than 0.5. There can be a different number of GWPs on both states with a minimum of one on each. In this work, up to 18 GWPs were used, nine on each state. Note that a full on-the-fly update of the LHA surfaces then corresponds to 36 frequency calculations. The initial wavepacket is thus a superposition of all these functions, with the expansion coefficients set to 0 for all functions on S_1 and S_0 except the function on S_1 centered at the FC point, which has a coefficient of 1. Due to the variational character of the method, the positioning of the initially unoccupied functions is not critical. They adapt as the wave function moves, and different choices affect only the detailed numerics and not the final result.

Initial explorations of the PESs were made using two GWPs, one on each diabatic electronic state (each GWP being a 5D Gaussian function). This minimal approach corresponds to an improved semiclassical picture, where the center of a GWP follows a trajectory described by classical equations of motion on its own diabatic surface plus a quantum contribution due to the other GWP, which becomes significant in regions where the off-diagonal term in the diabatic Hamiltonian matrix is large. Adding more GWPs in the expansion improves the results, as it allows the true quantum evolution of the wavepacket to be modeled better.

The case with one GWP on each state is easier to interpret in terms of transfer of electronic population. Only the diabatic GWP that starts off on S_1 is populated at time $t = 0$. A nonadiabatic transition happens when the two diabatic PESs cross along the trajectory followed by this diabatic GWP, thus swapping their respective S_0 or S_1 character. The resulting diabatic population is equal to the adiabatic population transferred to S_0 (nonadiabatic decay), once the wavepacket is sufficiently far from the nonadiabatic region. The transition is reactive if the wavepacket ends up on S_0 and keeps moving toward the prefulvenoid plateau (diabatic crossing) and is nonreactive if it further gets bounced back on S_0 and crosses back to S_1 benzene (diabatic trapping). Nonadiabatic transitions rarely are purely diabatic (populations will have finite values between 0 and 1). This implies that the second GWP that started on S_0 with a zero weight crosses from S_0 to S_1 with a nonzero weight (always observed in this work). In the case of a nonreactive transition, the second GWP will thus describe partial S_0 benzene regeneration (photophysics), while the first one describes partial diabatic trapping in S_1. In the case of a reactive transition, the first GWP will describe what was efficiently

transferred to S_0 (photochemistry), and the second one corresponds to what has been left in S_1.

4. The Extended Seam of Conical Intersection

The direct dynamics method, described above in section 3, generates a database of structures relevant to the dynamical properties of the system under study. Dynamics calculations on benzene led to a database of about 20 000 records (geometries and LHA representations of the S_0 and S_1 PESs). Only 42 records with an energy gap smaller than 0.5 eV were found. All of these 42 geometries corresponded to a half-chair prefulvenoid shape ($Q_{16x}/Q_4 = 1.3-1.7$, an almost constant ratio between the boat and chair deformations) and a wide-range distribution of size ($Q_1 = -0.7$ to 5.3, the dimensionless value of the breathing coordinate, with positive values corresponding to ring contraction from the S_0 minimum, i.e., FC point). A representative sample of nine geometries was selected and optimized to minimize the $S_1 - S_0$ energy difference and thus reach the closest point on the intersection seam. From each of the resulting geometries, a conical-intersection optimization was then carried out. In all cases, the optimizations smoothly led to the minimum of the seam ($Q_1 = 3.10$, $Q_4 = 6.28$, and $Q_{16x} = 8.16$), and no new critical points were found.

A mapping of the seam along Q_1 was also carried out. Starting from the minimum of the seam, the geometry was distorted by generating two extrapolated points where only the value of Q_1 was changed (increased and decreased) with respect to the minimum point. Both guess points were then optimized (in the full-dimensional space of nuclear coordinates) to minimize the $S_1 - S_0$ energy difference. From the two new points on the seam, the same process was repeated step-by-step to generate the next points uphill. More sophisticated methods, based on gradient techniques, are available for downhill searches of minimum-energy paths within intersection seams.[67−69] They were not used here, as we started the search from the minimum of the seam. For each point on the seam, the optimized value of Q_1 did not change by much with respect to the corresponding guess point. Results are displayed in Figure 4. The line obtained by this procedure is a cut through the 28-dimensional seam. The potential energy along the crossing line varies gently as a function of Q_1, which shows that all molecular *sizes* are quite accessible in terms of energy (see panel a in Figure 4). However, the prefulvenoid *shape* remains almost the same ($Q_{16x}/Q_4 = 1.3$). Except Q_1, all the coordinates remain almost constant and those that break the C_s symmetry remain zero.

The gradients of the two intersecting PESs were also calculated, as well as the $S_1 - S_0$ gradient difference and the gradient of the S_1/S_0 interstate coupling. In panel b in Figure 4, the mapping of the seam is plotted in the (Q_1, Q_4)-plane. The direction of the $S_1 - S_0$ gradient difference (projected onto this plane) is also represented for each calculated geometry, as well as the steepest-descent directions (negative of the gradients) on the two crossing PESs. Although this representation is limited to two dimensions, it gives the main features of the local topology of the conical intersection along the crossing line. For $Q_1 < 1.5$, the conical intersection is sloped: both steepest-descent directions lie on the same side of the seam (toward small values of Q_4, i.e., reactant side). For $Q_1 > 1.5$, the conical intersection is peaked: one steepest-descent direction leads back to the reactant (Q_4 decreases), while the other one leads to the product (Q_4 increases). Around the minimum of the seam ($Q_1 \approx 3$) the diabatic PES correlating the S_1 TS to prefulvene becomes almost flat.

This analysis confirmed that, as shown in a previous work,[16] the most important vibrations correspond to Q_1, Q_4, and Q_{16x} and to a smaller extent to Q_{6x} and Q_{18x} (in terms of C_s-preserving coordinates). The displacement from the FC point to any point of the crossing line is mostly expressed along these coordinates. In addition, these normal modes give the largest components of the directions of the S_1 and S_0 gradients and of the $S_1 - S_0$ gradient difference. Finally, the gradient of the interstate coupling (which, along with the $S_1 - S_0$ gradient difference, defines the local branching plane) defines a C_s-breaking direction that involves mostly Q_{15} (the Kékulé mode). The other two significant components are along Q_{14} and Q_{16y}. The latter was included in both reduced subspaces for dynamics (see Figure 3). Coordinate Q_{14} corresponds to the other Kékulé-like mode ($2b_{2u}$) that involves CCH bending rather than skeletal deformations. It is quite mixed with Q_{15}, as discussed in ref 16, and was not included in our description. Note also that, of course, the roles of the *x*- and *y*-components of a degenerate mode can be swapped, which in effect corresponds to describing another rotated version of the prefulvenoid species.

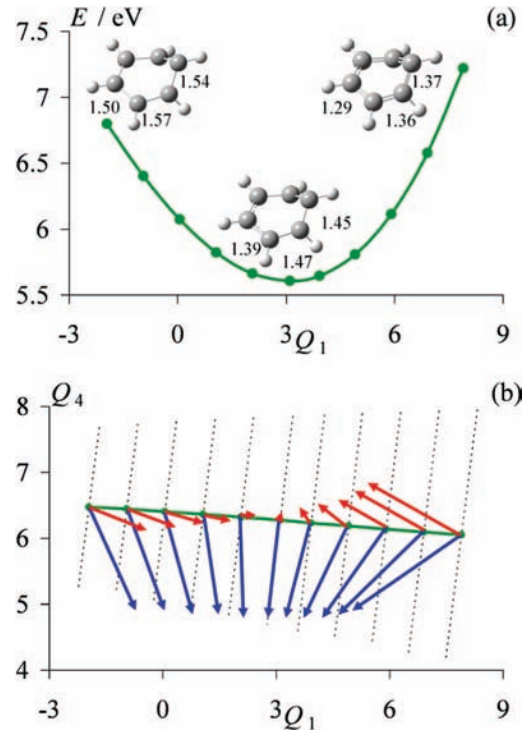

Figure 4. Cut-line through the S_1/S_0 seam of conical intersection mapped out along coordinate Q_1 (see Figure 3). (a) Degenerate potential energies along Q_1. (b) Trace of the line of degeneracy in the (Q_1, Q_4)-subspace of S_0 normal coordinates (frame origin, S_0 minimum, i.e., FC point). Blue and red arrows represent the negative of the gradients of the two intersecting PESs. Dashed lines represent the direction of the $S_1 - S_0$ gradient difference for each calculated point. CC bond lengths indicated on molecular structures (corresponding to $Q_1 = -1.95$, 3.10, and 7.90) are given in Å and illustrate variation in the *size*; the dihedral angle starting from the C nucleus that is out of the plane and following the connectivity of the next C nuclei ($C_1C_2C_3C_4$ in Figure 3) varies from to 43° to 40°, which illustrates preservation of the prefulvenoid *shape*.

5. Dynamical Exploration

To understand more systematically how to control the reactivity, depending on the nature of dynamical pathways leading to the seam, we ran quantum dynamical calculations and modulated the stimulation of photoactive modes in the initial conditions. Dynamical explorations were restricted to the 5D subspace defined in section 2 (see Figure 3), where all

coordinates but the five active ones remain fixed to zero. By varying the components of the **k** vector (mean initial momentum, see section 3) along the normal coordinates **Q** spanning the 5D subspace, it was possible to find conditions driving benzene on S_1 toward the intersection seam, thus inducing radiationless decay from S_1 to S_0 through nonadiabatic transitions. Increasing the magnitude of **k** is expected to favor a more diabatic behavior (a fast wavepacket starting on S_1, and going through a nonadiabatic region will transfer more population to S_0 than a slow wavepacket; reciprocally, there will be less transfer of population in the diabatic picture). More interesting is the influence of the direction of **k**.

Because of symmetry degeneracy, we can focus on the Q_{16x} (boat) coordinate rather than combinations of Q_{16x} and Q_{16y} (twist). These only change which of the three equivalent vertical mirror planes is preserved going from benzene to prefulvene. In addition, only positive momentum components k_4 and k_{16x} were considered, as the four quadrants are equivalent through nuclear permutation. Our choice corresponds to one of 12 degenerate paths leading from a given permutational version of D_{6h} benzene to the 12 chemically accessible versions of C_s prefulvene.

For a given mean energy, large $S_1 \rightarrow S_0$ population transfers were achieved when Q_4 and Q_{16x} were excited in a cooperative way to target values close to the projected S_1 TS point (see Table 1): $Q_4 = 5.14$ and $Q_{16x} = 7.20$ (the trajectory follows a prefulvenic direction, tangent to **k** at time $t = 0$). This also implies that the center of the GWP will further pass in the vicinity of the projected S_1/S_0 CoIn point (see Table 1, $Q_4 = 6.28$ and $Q_{16x} = 8.16$). Additionally, exciting Q_1 gives flexibility as to where the transition takes place on the projected seam (intersection between diabatic surfaces and avoided crossing between adiabatic surfaces). This is illustrated below by some selected cases. Note that an increase in the breathing-mode coordinate, Q_1, corresponds to a contraction of the ring.

Four cases with different initial **k** vectors are described in detail below. The four cases have in common an initial momentum given as $k_4 = 6.7$, $k_{16x} = 15.1$, and differ by $k_1 = 0$ (case A), 2.7 (case B), 2.9 (case C), and 4.3 (case D). Components of **k** not explicitly mentioned are initially set to zero. An illustrative example of **k** vector is represented in a $\{Q_1, Q_4, Q_{16x}\}$ cube in Figure 3 (lower panel). The dynamics from the simplest calculations with one GWP on each state (labeled 1 + 1) are straightforward to analyze by following the center of the initially populated GWP as shown in Figure 5, i.e., the "quantum trajectory" of the GWP that moves on the diabatic PES that correlates the FC region on S_1 to prefulvenoid structures on S_0. Note that the same characteristics dominate the better calculations using more GWPs (see below), especially in the motion toward the intersection region.

Figure 5 clearly shows the differences due to the initial conditions chosen. The four quantum trajectories are represented over 14 fs in three different planes of projection within the space of the five active coordinates, augmented by a potential energy axis. The main stationary points are also plotted. We focus here on the behavior of the end of the trajectories (after the transitions from S_1 to S_0, which roughly happen at the midpoint). Two types will be distinguished: reactive trajectories, which go in the direction of products (around the S_0 pF TS and S_0 Bv points), and nonreactive trajectories, which are bounced back toward the origin (geometry of the S_0 minimum), thus describing early photophysical deactivation.

Panel a corresponds to the geometrical plane spanned by coordinates Q_4 and Q_{16x}. Because the components of **k** are the same for the four trajectories in this plane, they appear superimposed. There, the region where nonadiabatic transitions take place is localized around the values of Q_4 and Q_{16x} at the geometry of the minimum of the conical intersection seam (the CoIn point in Table 1). The four trajectories are different with respect to the evolution of Q_1, because they correspond to different values of k_1. This is illustrated in panel b, which corresponds to the (Q_1, Q_4)-plane (note that negative values of Q_1 correspond to a ring expansion). There, the initial directions of the trajectories (tangent to **k**) make various angles with the Q_1-axis. The nonadiabatic region appears as a straight line, almost parallel to the Q_1-axis and characterized by the value of Q_4 at the CoIn point. The four trajectories will thus decay on S_0 at the same value of Q_4—and also Q_{16x}, following panel a—but different values of Q_1, i.e., same prefulvenoid shape but different size. Panel c is a representation of the reaction path of each trajectory, where the potential energy is plotted against Q_1. The symbols represent the diabatic potential energies (of the state connecting the S_1 FC point to the S_0 products). The corresponding adiabatic potential energies of S_1 (thick line) and S_0 (thin

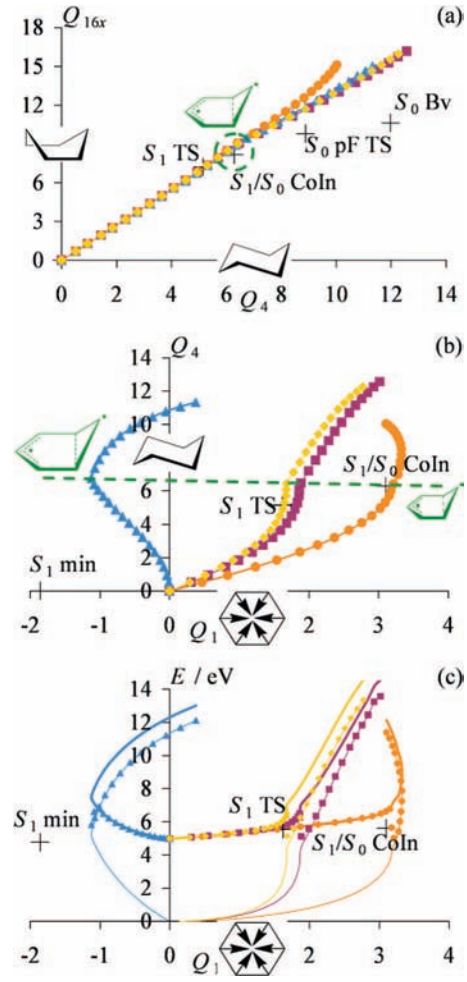

Figure 5. Four quantum trajectories differing by the value of the initial momentum k_1 along coordinate Q_1: case A, blue triangles; case B, yellow diamonds; case C, purple squares; case D, orange circles. (a) Projection in the (Q_4, Q_{16x})-subspace: dashed green circle, region where the nonadiabatic transition takes place. (b) Projection in the (Q_1, Q_4)-subspace: dashed green line, seam of intersection between diabatic states (prefulvenoid structures of various sizes, as indicated by green molecular structures). (c) Representation of the potential energy, noted as E and given in eV unit with respect to the S_0 minimum, of the quantum trajectories mapped along Q_1. In each plane, some projections of the critical points (see Table 1) are marked by plus signs.

line) are also shown at the same geometries for completeness. The three panels are views of the four trajectories on the PESs through two-dimensional faces of a four-dimensional hypercuboid (Q_1, Q_4, Q_{16x}, and E).

Case A serves as a reference, where $k_1 = 0$. This corresponds to an excess energy (above the FC point) of 8.4 eV. In the (Q_4, Q_{16x})-subspace (see panel a in Figure 5), the TS coordinates are reached after 6 fs when 1% of the population has been transferred to the lower electronic state. The CoIn coordinates are then reached between 7 and 7.5 fs. After 8.5 fs, the populations are stabilized and correspond to 50% on each electronic state.

It is interesting to note that case A shows an increase in Q_1 after the population transfer (see panel b in Figure 5) even if this mode was not initially stimulated. Since forming the products needs Q_1, Q_4, and Q_{16x} all to increase when the nonadiabatic transition occurs, this indicates that the trajectory tends to follow a path directed toward the product region after crossing from S_1 to S_0 (although the trajectory seems to curve, possibly starting to return to the reactant region).

To enhance this trend and make the nonadiabatic transition happen earlier and for positive values of Q_1, we added a positive component to **k** along Q_1 in cases B, C, and D. Cases B and C were found to be optimal, with less transfer of population than in case A but a stronger tendency to form the product. The larger value of k_1 in case D was found to be counterproductive because of the presence of the S_1 TS barrier on the way to the crossing region.

Case B ($k_1 = 2.7$, excess energy 8.8 eV) corresponds to targeting the TS coordinates at 6 fs ($Q_1 = 1.62$), and case D ($k_1 = 4.3$, excess energy 9.6 eV) corresponds to targeting directly those of the CoIn ($Q_1 = 3.10$). Case C ($k_1 = 2.9$, excess energy 8.9 eV) is in between. These three cases exhibit populations of about 33% on S_0 after the transition. For cases B and C, the trajectories go in the direction of the products on average (note that the S_0 pF TS and Bv points are not represented in panel b of Figure 5, because they are out of range with respect to the Q_1 coordinate). Thus, although cases B and C produce a less efficient population transfer than case A, the efficiency for producing the desired product (S_0 Bv in Table 1 and Figure 5) should be increased. In contrast, case D, which crossed from S_1 to S_0 around the projection of the CoIn point within the 5D subspace, hits a turning point when exploring further the S_0 PES (see panel c in Figure 5). This "bobsled" effect (the wavepacket slides on the side walls of the half-pipe in the PES around the S_1 TS) makes the trajectory curve back toward the reactant region. Thus, efficient formation of the product is expected from trajectories that go through a region around the TS (cases B and C) but not closer to the CoIn. Case C, which passes to one side of the TS coordinates, actually seems better than case B because it leads to lower parts of the S_0 PES beyond the nonadiabatic transition.

The topology of the accessible part of the seam described in section 4 is consistent with what was observed in the dynamics simulations. All crossing geometries are prefulvenoid (narrow range of values for the chair and boat coordinates) but with various sizes (large range of values for the breathing coordinate). The crossing is sloped for dilated structures (left-hand side on panel b in Figure 4). This corresponds to case A (see Figure 5), where the trajectory has enough energy to cross but is further deflected to the right-hand side (risk of being bounced back to the reactant). Around $Q_2 = 1.5$ (value of Q_1 at the S_1 TS), the crossing starts to become peaked. This corresponds to the optimal cases B and C (see Figure 5), where the trajectories

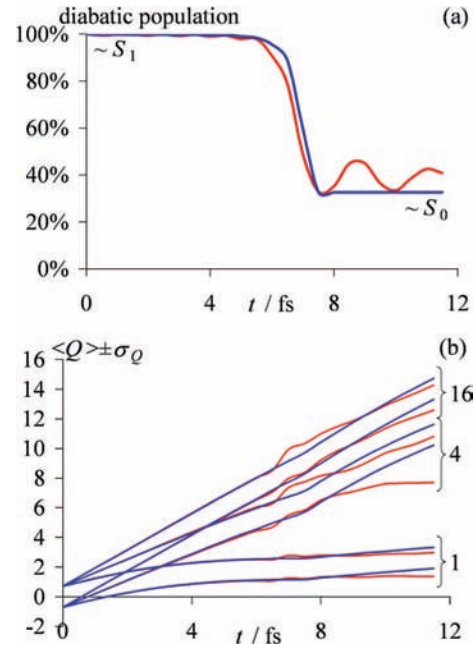

Figure 6. Comparison over 11.5 fs of 1 + 1 GWP (blue lines) and 5 + 5 GWP (red lines) calculations for case C. (a) Population of the diabatic component starting on S_1 and transferred to S_0. (b) Expectation value of Q_j ($j = 1$, 4, and 16x as indicated on the right of the curves) plus and minus the corresponding standard deviation (which is a constant equal to $2^{-1/2}$ in the 1 + 1 GWP case).

have passed without deviation over the TS and can continue further beyond the crossing to form the product. The crossing is still peaked for even more compact structures (right-hand side of panel b in Figure 4). Case D (see Figure 5) was prepared to target the minimum of the seam ($Q_1 \approx 3$). Crossing here should be optimal: the potential energy is lower and the slope leads to prefulvene. However, the trajectory arrives here with a counterproductive momentum direction (deflection to the left-hand side) because of a bobsled effect induced by the curvature of the PES when the trajectory slides on the side walls of the TS. This effect should be even stronger beyond ($Q_1 > 3$), because the steepest-descent directions along the crossing line also lead to the left-hand side (more deflection). The agreement, between the full-dimensional static study of the topography and the dynamics simulations in reduced dimension, shows that our 5D model is relevant for describing the main features of the nonadiabatic process.

The 1 + 1 calculations are quite crude in terms of describing quantum effects. We checked that a more refined calculation based on case C but using 5 GWPs on each state (5 + 5) showed the same trend before the crossing and a more complicated behavior after the crossing (see Figure 6), as expected. The diabatic populations (Figure 6a) evolve similarly except for a damped oscillation (~2 fs period) present in the 5 + 5 calculation due to the more complicated interactions between the parts of the wavepacket now possible. Panel b in Figure 6 depicts the time evolution of the average (wavepacket center), plus or minus the standard deviation (wavepacket width) for modes 1, 4, and 16x in both the 1 + 1 and 5 + 5 calculations. This shows that the path from the FC region to the crossing (up to 6 fs) does not depend on the number of GWPs in the expansion, either for the center or for the width of the wavepacket. The most significant change in the wavepacket evolution is seen after the crossing for the chair (Q_4) and Kékulé (Q_{15}) modes. With respect to case C, the average value of Q_4 is slowed down (multiplied by ~0.85 at $t = 11.5$ fs) while the

corresponding width increases quite fast (multiplied by ~2.2 at $t = 11.5$ fs). It is also worth mentioning that the deflection along the derivative coupling, marked here by nonzero values of the average of Q_{15} after the transition, is weaker with this more quantum description, and the corresponding width increases dramatically after the crossing: the bifurcation of the wavepacket can now be described by trajectories running on either side of the side slopes of the uphill cone, leading to a symmetrical spreading of the wavepacket. This is the quantum mechanical equivalent of the nonadiabatic deflection experienced by semiclassical trajectories along the direction of the derivative coupling.

We now mention briefly results using other directions for the initial **k** vector. A case with only $k_{16x} = 15.1$ gives 10% of population transfer, which happens at $Q_1 \approx 0$ and $Q_{16x} \approx 15$, i.e., at geometries related to a stretched Dewar benzene ($Q_1 = 8.84$ and $Q_{16x} = 14.31$). However, the subsequent evolution of the wavepacket describes a deactivation pathway toward benzene (photostability) rather than a possible pathway to Dewar benzene production. Interestingly enough, this case exhibits strong IVR from Q_{16x} to Q_1, which in our experience is a constant feature. A case with only $k_4 = 6.7$ shows no nonadiabatic behavior at all. Other directions were targeted with the same excess energy as case A. For example, using $k_4 = 10.0$ and $k_{16x} = 11.6$ or $k_4 = 13.0$ and $k_{16x} = 4.4$ led to nonreactive population transfers, because they occur when Q_1 is negative and decreasing.

Choosing large values for the **k** components simplifies the problem for two reasons: first, the beginning of the trajectory in the (Q_4, Q_{16x})-subspace is linearized along the direction of the initial momentum; second, the diabatic behavior is enhanced, thus magnifying the effect of the nonadiabatic coupling between S_1 and S_0. The electronic PESs, which are reasonably well behaved in the 5D subspace before the crossing, tend to rise up very steeply after the crossing (see Figure 5c), because the system becomes far too rigid. Thus, access to the nonadiabatic region is reasonably described in this reduced space, whereas conclusions about the outcome of the trajectory after the transition from S_1 to S_0 should be drawn carefully.

Beyond the crossing, more degrees of freedom are required to make the system flexible enough. A 9D model, detailed in the Supporting Information, was shown to enable a better description of the reaction coordinate leading to products through the S_1 transition barrier (prefulvenic CC bond formation; see Scheme 1 and Figure 1). We checked that 9D trajectories, run under similar conditions to 5D trajectories, led to a similar dynamical behavior before the crossing. Beyond the transition barrier the PESs are, however, less steep in 9D, allowing larger amplitude motions for a given excess energy initially deposited in the (Q_1, Q_4, and Q_{16x})-subspace. A 9D calculation similar to case C is described in the Supporting Information.

6. Controlling the Pathways

A final set of calculations used a sequence of "kicks", each corresponding to the excitation of a single mode with suitable delays, so that all modes reach their respective extrema at about the same time. Calculations were run in the 9D subspace. The first excitation was the Herzberg−Teller[43] active mode Q_{6x} with a target time of 43 fs (about one and a half-oscillations), then Q_{16x}, Q_4, and finally Q_{18x} (see Figure 7). Controlling the breathing mode Q_1 directly proved to be difficult, as IVR from out-of-plane modes severely complicates the motion of this mode. As a result, no additional momentum was added to this mode, and it was simply checked that both Q_1 and k_1 took positive values at target time.

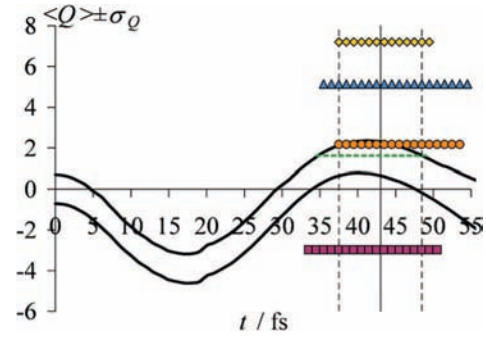

Figure 7. Control strategy using a sequence of delayed kicks. The pair of black curves shows the time evolution of the wavepacket along Q_1 as the expectation value plus/minus the corresponding standard deviation. The horizontal green dashes correspond to the value of Q_1 at the S_1 TS, plotted for the time interval during which the wavepacket covers this space interval. The same kind of target intervals are represented for Q_4 (blue triangles), Q_{6x} (purple squares), Q_{16x} (yellow diamonds), and Q_{18x} (orange circles). The vertical black line figures the target time (43 fs), and the vertical dashed lines (at 37.5 and 48.5 fs) denote the time interval of overlap between the five target intervals, i.e., when the wavepacket is at the target. This case was calculated in the 9D subspace with 9 GWPs on each electronic state. The sequence of single-mode impulsions corresponds to $k_{6x} = 2.7$, initially, and then $k_{16x} = 5.1$ at $t = 16$ fs, $k_4 = 3.0$ at $t = 21$ fs and $k_{18x} = 1.2$ at $t = 33$ fs.

Using nine GWPs for each state, conditions were found with which it is possible to drive the normal modes to their values at the transition barrier at target time. This was taken as 43 ± 5.5 fs by considering as a tolerance range the expectation value of Q_j plus or minus the standard deviation, for $j = 1$, 4, 6x, 16x, and 18x. The trajectory along Q_1 is shown in Figure 7. The total energetic cost is now 2.04 eV, much lower than the energy input in the single-kick cases above. Such conditions transfer just enough excess energy to Q_1 to reach its value at the TS. More energy is thus required to pass beyond the barrier rather than to be bounced back.

A single initial kick is energetically expensive, as a part of the excess energy is wasted in unnecessary large oscillations of the slower modes. As shown here, a better strategy is to introduce a delay between excitations of specific modes, one at a time. The energies of the kicks used in the calculations are in general much higher than achievable experimentally. There are two reasons for this. The first is due to the simple CASSCF treatment used, which overestimates the values for excited states. The second is the use of a reduced dimensionality model, which effectively raises the steepness of the PES by its rigidity. A more flexible description should open alternative accessible pathways where less excess energy is necessary to cross the seam and form products. With more degrees of freedom, IVR is also expected to transfer part of the kinetic energy to other modes, thus cooling the deformation modes the most involved in following the reaction path. Despite this, the study shows that it should be possible to find initial conditions that give access to efficient and direct pathways leading from the FC region to the prefulvenoid plateau on the ground state.

7. Conclusions and Outlook

The work presented above used a methodology designed for efficient direct quantum dynamics calculations on systems of interest in organic photochemistry that are not accessible to study by conventional grid-based quantum dynamics. The capabilities of the vMCG method have been demonstrated recently in benchmark calculations on the pyrazine absorption spectrum.[70]

For a 4-dimensional subsystem, not only the spectrum but also the more sensitive autocorrelation function is converged with respect to the full quantum dynamics with 160 GWPs. In contrast, if the GWPs are bound to follow classical trajectories, convergence is not reached even with 1000 functions. The direct dynamics implementation, DD-vMCG, [27−30] gives access to quantum dynamics for large systems by combining on-the-fly evaluation of the PES at the LHA level and an ever-growing database to reduce computation time by avoiding redundant ab initio calculations. In some works in progress, short simulations (less than 100 fs) have been run on a 39-dimensional system and another 6-dimensional system has been studied for as long as 0.6 ps. However, one must accept that such calculations are currently limited by the accuracy of quantum chemistry methods capable of providing analytical second derivatives of the energy, viz., CASSCF.

In this work, the final database contained about 20 000 accumulated records stored on 800 Mb, each of them made up of a geometry and the corresponding pair of potential energies, gradients, and Hessians for the ground and the first excited state of C_6H_6 at the CASSCF(6,6)/6-31G* level, sometimes with 0.5:0.5 state-averaging depending on the energy gap. In addition to saving time, this methodology provides a reservoir of ab initio data at the end of the study that can be used for subsequent work. Such data are valuable and would help in the building of a fitted representation of the PES in the important region to describe the physicochemical phenomenon under study. Full database convergence (i.e., no further quantum chemistry calculation required) was never reached, but the effective number of ab initio calculations was noticeably reduced in most cases.

Reduced dimensionality models of benzene were used to simplify the description and get insights into the main features of nonadiabatic transitions from S_1 to S_0 in terms of internal motion. Models were defined using a limited number of relevant deformation modes, carefully chosen using both static data and dynamical properties.[16] Some coordinates are obvious if they describe features of the coupled PESs at first-order: in particular, the directions of the FC gradient and of the vectors of the branching space at the minimum of the seam. The rest are to be understood as second-order effects that involve curvatures and changes of shape, allowing for a more extended picture of the energetic landscape. For simplicity, normal coordinates frozen at the S_0 equilibrium geometry were used. Prefulvenoid species and benzvalene can be derived from benzene via global and fairly compact deformations around the molecular plane, so curvilinear coordinates were not needed here.

In the context of intelligent control, theory must help experiment by finding an easy and relevant target early on in the mechanism. Only then can we expect to rationalize optimal control in large systems. In our study, we ignored Herzberg−Teller vibronic selection rules for this vibronically induced "forbidden" transition,[43] and CASSCF energies are often too high compared to experiments. However, our static and quantum dynamics simulations can be viewed as a proof of concept that controlling the photoreactivity of benzene seems plausible, because an energetically accessible part of the intersection seam can be extended along the breathing mode coordinate, leading thus to many different structures where internal conversion can proceed.

Along this seam, our calculations show that the topology changes from a sloped conical intersection at high energy to a peaked conical intersection toward the minimum of the seam. Coming from the FC point, the slopes of the intersecting PESs are both uphill in the sloped region, such that radiationless decay to the ground state will favor reactant regeneration (photophysics). However, ground-state prefulvene lies beyond a peaked intersection, and forming this needs radiationless decay to occur in this region (photochemistry), eventually leading to production of benzvalene (see Figure 2 and, e.g., refs 12, 22, and 23−25 for similar mechanistic principles applied to various systems). This is to be weighted by the presence of a transition barrier in front of the seam, which defines an effective range of "shooting lines": from the FC point, targeting the seam with a straight shot (a initial momentum kick) requires passing in the vicinity of the S_1 TS for the trajectory to lead to products. It is thus better to design initial conditions that will drive the system to cross the seam possibly at a higher point than the minimum, in line with the transition region as viewed from the FC point. Such topological arguments, supported by quantum dynamics explorations, can be used to control benzene photochemistry if experimental conditions (accounting for selection rules) can be designed to target specific structures on this extended seam of conical intersection. The initial conditions used in this work (kick in the form of a momentum given to an intial FC wavepacket) cannot yet be achieved experimentally. A work is in progress in which we modulated the spatial distribution of the initial wavepacket along relevant modes, according to specific vibronic transitions that can be excited by a tailored laser pulse. This model study applied to benzene as a test case suggests general strategies for intelligent laser-driven control of photochemistry.

Acknowledgment. Special thanks are due to Dr. I. Burghardt for collaboration in the theoretical and algorithmic aspects of this work. The authors are indebted to Dr. M. Boggio-Pasqua for discussions. B.L. acknowledges financial support by EPSRC (Grant No: GR/T20311/01).

Supporting Information Available: (i) The vMCG equations of motion (details on the formalism), (ii) database implementation (details on the algorithm and the transformations to a reference frame), and (iii) 9D simulations (with one additional figure and extended versions of Figure 3 and Table 1).This material is available free of charge via the Internet at http://pubs.acs.org.

References and Notes

(1) Rice, S. A.; Zhao, M. *Optical Control of Molecular Dynamics*; Wiley: New York, 2000.
(2) Shapiro, M.; Brumer, P. *Principles of the Quantum Control of Molecular Processes*; Wiley: New York, 2003.
(3) May, V.; Kühn, O. *Charge and Energy Transfer Dynamics in Molecular Systems*, 2nd ed.; Wiley-VCH: Berlin, 2004.
(4) Tannor, D. J.; Rice, S. A. *J. Chem. Phys.* **1985**, *83*, 5013.
(5) Judson, R. S.; Rabitz, H. *Phys. Rev. Lett.* **1992**, *68*, 1500.
(6) Daniel, C.; Full, J.; Gonzalez, L.; Lupulescu, C.; Manz, J.; Merli, A.; Vajda, S.; Woste, L. *Science* **2003**, *299*, 536.
(7) Zou, S. Y.; Ren, Q. H.; Balint-Kurti, G. G.; Manby, F. R. *Phys. Rev. Lett.* **2006**, *96*, 243003.
(8) Dietzek, B.; Bruggemann, B.; Pascher, T.; Yartsev, A. *Phys. Rev. Lett.* **2006**, *97*, 258301.
(9) Hunt, P. A.; Robb, M. A. *J. Am. Chem. Soc.* **2005**, *127*, 5720.
(10) *Conical Intersections: Electronic Structure, Dynamics & Spectroscopy*; Domcke, W., Yarkony, D. R., Köppel, H., Eds.; World Scientific: Singapore, 2004.
(11) Boggio-Pasqua, M.; Ravaglia, M.; Bearpark, M. J.; Garavelli, M.; Robb, M. A. *J. Phys. Chem. A* **2003**, *107*, 11139.
(12) Paterson, M. J.; Robb, M. A.; Blancafort, L.; DeBellis, A. D. *J. Phys. Chem. A* **2005**, *109*, 7527.
(13) Migani, A.; Gentili, P. L.; Negri, F.; Olivucci, M.; Romani, A.; Favaro, G.; Becker, R. S. *J. Phys. Chem. A* **2005**, *109*, 8684.
(14) Meyer, H. D.; Le Quere, F.; Leonard, C.; Gatti, F. *Chem. Phys.* **2006**, *329*, 179.

(15) Richter, F.; Gatti, F.; Leonard, C.; Quere, F. L.; Meyer, H.-D. *J. Chem. Phys.* **2007**, *127*, 164315.
(16) Lasorne, B.; Sicilia, F.; Bearpark, M. J.; Worth, G. A.; Blancafort, L.; Robb, M. A. *J. Chem. Phys.* **2008**, *128*, 124307.
(17) Palmer, I. J.; Ragazos, I. N.; Bernardi, F.; Olivucci, M.; Robb, M. A. *J. Am. Chem. Soc.* **1993**, *115*, 673.
(18) Riedle, E.; Weber, T.; Schubert, U.; Neusser, H. J.; Schlag, E. W. *J. Chem. Phys.* **1990**, *93*, 967.
(19) Lee, S. A.; White, J. M.; Noyes, W. A. *J. Chem. Phys.* **1976**, *65*, 2805.
(20) Smith, B. R.; Bearpark, M. J.; Robb, M. A.; Bernardi, F.; Olivucci, M. *Chem. Phys. Lett.* **1995**, *242*, 27.
(21) Domcke, W.; Sobolewski, A. L.; Woywod, C. *Chem. Phys. Lett.* **1993**, *203*, 220.
(22) Bearpark, M. J.; Bernardi, F.; Clifford, S.; Olivucci, M.; Robb, M. A.; Smith, B. R.; Vreven, T. *J. Am. Chem. Soc.* **1996**, *118*, 169.
(23) Migani, A.; Bearpark, M. J.; Olivucci, M.; Robb, M. A. *J. Am. Chem. Soc.* **2007**, *129*, 3703.
(24) Hall, K. F.; Boggio-Pasqua, M.; Bearpark, M. J.; Robb, M. A. *J. Phys. Chem. A* **2006**, *110*, 13591.
(25) Boggio-Pasqua, M.; Robb, M. A.; Bearpark, M. J. *J. Phys. Chem. A* **2005**, *109*, 8849.
(26) Worth, G. A.; Robb, M. A.; Burghardt, I. *Faraday Discuss.* **2004**, *127*, 307.
(27) Lasorne, B.; Bearpark, M. J.; Robb, M. A.; Worth, G. A. *Chem. Phys. Lett.* **2006**, *432*, 604.
(28) Lasorne, B.; Robb, M. A.; Worth, G. A. *Phys. Chem. Chem. Phys.* **2007**, *9*, 3210.
(29) Lasorne, B.; Worth, G. A. Direct dynamics with quantum nuclei. In *The MCTDH Method*; Meyer, H. D., Gatti, F., Worth, G. A., Eds.; Wiley-VCH: Weinheim, 2008; in preparation.
(30) Worth, G. A.; Lasorne, B.; Robb, M. A. *Mol. Phys.* **2008**, in press.
(31) Lauvergnat, D.; Baloitcha, E.; Dive, G.; Desouter-Lecomte, M. *Chem. Phys.* **2006**, *326*, 500.
(32) Gatti, F.; Justum, Y.; Menou, M.; Nauts, A.; Chapuisat, X. *J. Mol. Spectrosc.* **1997**, *181*, 403.
(33) Gatti, F. *Chem. Phys. Lett.* **2003**, *373*, 146.
(34) Lauvergnat, D.; Nauts, A. *J. Chem. Phys.* **2002**, *116*, 8560.
(35) Gindensperger, E.; Burghardt, I.; Cederbaum, L. S. *J. Chem. Phys.* **2006**, *124*, 144103.
(36) Paterson, M. J.; Bearpark, M. J.; Robb, M. A.; Blancafort, L. *J. Chem. Phys.* **2004**, *121*, 11562.
(37) Paterson, M. J.; Bearpark, M. J.; Robb, M. A.; Blancafort, L.; Worth, G. A. *Phys. Chem. Chem. Phys.* **2005**, *7*, 2100.
(38) Sicilia, F.; Blancafort, L.; Bearpark, M. J.; Robb, M. A. *J. Phys. Chem. A* **2007**, *111*, 2182.
(39) Sicilia, F.; Bearpark, M. J.; Blancafort, L.; Robb, M. A. *Theor. Chem. Acc.* **2007**, *118*, 241.
(40) Shaik, S.; Shurki, A.; Danovich, D.; Hiberty, P. C. *J. Am. Chem. Soc.* **1996**, *118*, 666.
(41) Blancafort, L.; Sola, M. *J. Phys. Chem. A* **2006**, *110*, 11219.
(42) Wilson, E. B. *Phys. Rev.* **1934**, *45*, 706.
(43) Atkinson, G. H.; Parmenter, C. S. *J. Mol. Spectrosc.* **1978**, *73*, 31.
(44) Worth, G. A.; Bearpark, M. J.; Robb, M. A. Semiclassical Nonadiabatic Trajectory Computations In Photochemistry: Is The Reaction Path Enough To Understand A Photochemical Reaction Mechanism? In *Computational Photochemistry*; Olivucci, M., Ed.; Elsevier: Amsterdam, 2005; pp 171.
(45) Meyer, H. D.; Manthe, U.; Cederbaum, L. S. *Chem. Phys. Lett.* **1990**, *165*, 73.
(46) Manthe, U.; Meyer, H. D.; Cederbaum, L. S. *J. Chem. Phys.* **1992**, *97*, 3199.
(47) Beck, M. H.; Jäckle, A.; Worth, G. A.; Meyer, H. D. *Phys. Rep.* **2000**, *324*, 1.
(48) Meyer, H. D.; Worth, G. A. *Theor. Chem. Acc.* **2003**, *109*, 251.
(49) Manthe, U. *J. Chem. Phys.* **2008**, *128*, 064108.
(50) Vendrell, O.; Gatti, F.; Meyer, H. D. *Angew. Chem.-Int. Ed.* **2007**, *46*, 6918.
(51) Vendrell, O.; Gatti, F.; Lauvergnat, D.; Meyer, H. D. *J. Chem. Phys.* **2007**, *127*, 184302.
(52) Vendrell, O.; Gatti, F.; Meyer, H. D. *J. Chem. Phys.* **2007**, *127*, 184303.
(53) Coutinho-Neto, M. D.; Viel, A.; Manthe, U. *J. Chem. Phys.* **2004**, *121*, 9207.
(54) Cattarius, C.; Worth, G. A.; Meyer, H. D.; Cederbaum, L. S. *J. Chem. Phys.* **2001**, *115*, 2088.
(55) Raab, A.; Worth, G. A.; Meyer, H. D.; Cederbaum, L. S. *J. Chem. Phys.* **1999**, *110*, 936.
(56) Heller, E. J. *J. Chem. Phys.* **1975**, *62*, 1544.
(57) Worth, G. A.; Robb, M. A. *Adv. Chem. Phys.* **2002**, *124*, 355.
(58) Ben-Nun, M.; Martínez, T. J. *Chem. Phys.* **2000**, *259*, 237.
(59) Martínez, T. J. *Acc. Chem. Res.* **2006**, *39*, 119.
(60) Ben-Nun, M.; Martínez, T. J. *Adv. Chem. Phys.* **2002**, *121*, 439.
(61) Ben-Nun, M.; Quenneville, J.; Martínez, T. J. *J. Phys. Chem. A* **2000**, *104*, 5161.
(62) Worth, G. A.; Beck, M. H.; Jäckle, A.; Meyer, H. D. *The MCTDH Package, Development Version 9.0*, University of Heidelberg: Heidelberg, Germany, 2006; see http://www.pci.uni-heidelberg.de/tc/usr/mctdh/.
(63) Worth, G. A.; Burghardt, I. *Chem. Phys. Lett.* **2003**, *368*, 502.
(64) Burghardt, I.; Meyer, H. D.; Cederbaum, L. S. *J. Chem. Phys.* **1999**, *111*, 2927.
(65) Köppel, H.; Gronki, J.; Mahapatra, S. *J. Chem. Phys.* **2001**, *115*, 2377.
(66) Frisch, M. J.; Trucks, G. W.; Schlegel, H. B.; Scuseria, G. E.; Robb, M. A.; Cheeseman, J. R.; Montgomery, J. A., Jr.; Vreven, T.; Kudin, K. N.; Burant, J. C.; Millam, J. M.; Iyengar, S. S.; Tomasi, J.; Barone, V.; Mennucci, B.; Cossi, M.; Scalmani, G.; Rega, N.; Petersson, G. A.; Nakatsuji, H.; Hada, M.; Ehara, M.; Toyota, K.; Fukuda, R.; Hasegawa, J.; Ishida, M.; Nakajima, T.; Honda, Y.; Kitao, O.; Nakai, H.; Klene, M.; Li, X.; Knox, J. E.; Hratchian, H. P.; Cross, J. B.; Bakken, V.; Adamo, C.; Jaramillo, J.; Gomperts, R.; Stratmann, R. E.; Yazyev, O.; Austin, A. J.; Cammi, R.; Pomelli, C.; Ochterski, J. W.; Ayala, P. Y.; Morokuma, K.; Voth, G. A.; Salvador, P.; Dannenberg, J. J.; Zakrzewski, V. G.; Dapprich, S.; Daniels, A. D.; Strain, M. C.; Farkas, O.; Malick, D. K.; Rabuck, A. D.; Raghavachari, K.; Foresman, J. B.; Ortiz, J. V.; Cui, Q.; Baboul, A. G.; Clifford, S.; Cioslowski, J.; Stefanov, B. B.; Liu, G. L., A.; Piskorz, P. K., I.; Martin, R. L.; Fox, D. J.; Keith, T.; Al-Laham, M. A.; Peng, C. Y.; Nanayakkara, A.; Challacombe, M.; Gill, P. M. W.; Johnson, B.; Chen, W.; Wong, M. W.; Gonzalez, C.; Pople, J. A. *Gaussian Development Version, Revision B.07; Development Version, Revision B.07*; Gaussian, Inc.: Pittsburgh, PA, 2003.
(67) Migani, A.; Robb, M. A.; Olivucci, M. *J. Am. Chem. Soc.* **2003**, *125*, 2804.
(68) Weingart, O.; Migani, A.; Olivucci, M.; Robb, M. A.; Buss, V.; Hunt, P. *J. Phys. Chem. A* **2004**, *108*, 4685.
(69) Sicilia, F.; Blancafort, L.; Bearpark, M. J.; Robb, M. A. *J. Chem. Theory Comput.* **2008**, *4*, 257.
(70) Burghardt, I.; Giri, K.; Worth, G. A. *J. Chem. Phys.* **2008**, submitted.

JP803740A